

A multi-parametric particle-pairing algorithm for particle tracking in single and multiphase flows

This article has been downloaded from IOPscience. Please scroll down to see the full text article.

2011 Meas. Sci. Technol. 22 105406

(<http://iopscience.iop.org/0957-0233/22/10/105406>)

View [the table of contents for this issue](#), or go to the [journal homepage](#) for more

Download details:

IP Address: 107.4.138.78

The article was downloaded on 27/08/2011 at 15:55

Please note that [terms and conditions apply](#).

A multi-parametric particle-pairing algorithm for particle tracking in single and multiphase flows

Nicholas D Cardwell¹, Pavlos P Vlachos¹ and Karen A Thole²

¹ Mechanical Engineering Department, Virginia Polytechnic Institute and State University, Blacksburg, VA 24061, USA

² Mechanical and Nuclear Engineering Department, Pennsylvania State University, University Park, PA 16802, USA

E-mail: pvlachos@vt.edu

Received 5 January 2011, in final form 17 July 2011

Published 26 August 2011

Online at stacks.iop.org/MST/22/105406

Abstract

Multiphase flows (MPFs) offer a rich area of fundamental study with many practical applications. Examples of such flows range from the ingestion of foreign particulates in gas turbines to transport of particles within the human body. Experimental investigation of MPFs, however, is challenging, and requires techniques that simultaneously resolve both the carrier and discrete phases present in the flowfield. This paper presents a new multi-parametric particle-pairing algorithm for particle tracking velocimetry (MP3-PTV) in MPFs. MP3-PTV improves upon previous particle tracking algorithms by employing a novel variable pair-matching algorithm which utilizes displacement preconditioning in combination with estimated particle size and intensity to more effectively and accurately match particle pairs between successive images. To improve the method's efficiency, a new particle identification and segmentation routine was also developed. Validation of the new method was initially performed on two artificial data sets: a traditional single-phase flow published by the Visualization Society of Japan (VSJ) and an in-house generated MPF data set having a bi-modal distribution of particles diameters. Metrics of the measurement yield, reliability and overall tracking efficiency were used for method comparison. On the VSJ data set, the newly presented segmentation routine delivered a twofold improvement in identifying particles when compared to other published methods. For the simulated MPF data set, measurement efficiency of the carrier phases improved from 9% to 41% for MP3-PTV as compared to a traditional hybrid PTV. When employed on experimental data of a gas–solid flow, the MP3-PTV effectively identified the two particle populations and reported a vector efficiency and velocity measurement error comparable to measurements for the single-phase flow images. Simultaneous measurement of the dispersed particle and the carrier flowfield velocities allowed for the calculation of instantaneous particle slip velocities, illustrating the algorithm's strength to robustly and accurately resolve polydispersed MPFs.

Keywords: particle tracking velocimetry, particle image velocimetry

(Some figures in this article are in colour only in the electronic version)

Nomenclature

General

A_p	particle area
C_{12}	particle-matching coefficient
d	particle diameter
D	number of measured vectors
e_{xy}	average position error, $e_{xy} = \frac{1}{n_I} \sqrt{(x_m(i) - x_a)^2 + (y_m(i) - y_a)^2}$
$e_{RMS,xy}$	root mean square deviation of position error, $e_{RMS,xy} = \sqrt{\frac{1}{n_I} \sum_{i=1}^{n_I} (e_{xy}(i) - e_{xy})^2}$
e_{uv}	average vector error, $e_{uv} = \frac{1}{N} \sum_{i=1}^N \sqrt{(u_m(i) - u_a)^2 + (v_m(i) - v_a)^2}$
$e_{RMS,uv}$	root mean square deviation of vector error, $e_{RMS,uv} = \sqrt{\frac{1}{N} \sum_{i=1}^N (e_{uv}(i) - e_{uv})^2}$
E_Y	vector yield, $E_Y = D/V$
E_R	vector reliability, $E_R = N/D$
E_F	measurement efficiency, $E_F = E_Y \times E_R$
I, I_{xy}	pixel intensity value
I_s, I_{exp}	intensity value of the source and expanding pixel, respectively
I_{th}	intensity threshold level
n_I	number of identified particles
n_k	number of known particles
n_S	number of sized particles
N	number of correct vectors
p_{num}	particle ID number
r_S	search radius
$U_{slip}, V_{slip}, Vel_{slip}$	slip velocity, $U_{slip} = u_{sand} - u_{tracer}$, $V_{slip} = v_{sand} - v_{tracer}$, $Vel_{slip} = \sqrt{U_{slip}^2 + V_{slip}^2}$
V	number of known vectors
W_d, W_I, W_{NN}	pair-matching parameter weights
u, v	velocity variables
x, y	spatial variables

Greek

σ	population standard deviation
σ_S	number of standard deviations to calculate diameter (from [7])
ΔVel	velocity difference, $\Delta Vel = (\sqrt{u^2 + v^2})_{PIV} - (\sqrt{u^2 + v^2})_{MP3} $

Identification methods

SVT	single value threshold
EDT	erosion/dilation threshold

Sizing methods

IWC	intensity weighted centroid
TPG	three-point Gaussian

FPG	four-point Gaussian
CFPG	continuous four-point Gaussian
LSG	least-squares Gaussian
CLSG	continuous least-squares Gaussian

Tracking methods

NN	single component—nearest neighbor
NN-d	two component—NN and particle diameter
NN-I	two component—NN and max intensity
NN-d-I	three component—NN, particle diameter and max intensity

1. Introduction

The investigation of multiphase flows (MPFs) is of considerable interest to the scientific and engineering community. Despite numerous advancements in the field, there is still a need for robust non-invasive experimental techniques tailored toward MPFs. The desired method would be able to simultaneously resolve the velocity of the carrier and discrete phases as well as providing size and shape information for the discrete phase [3, 4, 24]. Phase Doppler particle analyzer (PDA/PDPA) was traditionally used for simultaneous velocity and size measurements. However, PDPA is limited by the assumption of spherical droplets/particles [6, 16] and is a point measurement technique.

For spatiotemporally resolved measurements, particle image velocimetry (PIV) and particle tracking velocimetry (PTV) have gained wide acceptance in MPFs [13, 14]. However, traditional PIV/PTV analysis is often based on the assumption that the particles resolved behave approximately as flow tracers, which in most cases is not applicable under realistic MPF conditions. In this work, we develop and present a methodology that overcomes this limitation and significantly augments the capability and accuracy of PTV/PIV analysis toward resolving complex MPFs, with special consideration to the case when the dispersed phase does not follow the main flow. Such conditions often impose insurmountable challenges for conventional PTV/PIV methods.

PIV [1, 37, 39] employs a locally windowed cross-correlation between two successive images to determine the displacement of particle patterns. While it is effective in the measurement of single-phase flows, the extension of PIV to measuring MPFs is very challenging, especially when the motion of the carrier and discrete phases do not correlate well with one another. Moreover, the local velocity estimation tends to be biased toward the velocity of the largest and brightest particles within the pattern.

PTV, unlike PIV, relies on the direct tracking of individual particles between successive images. By this methodology, the motions of each phase may therefore be measured independently of the other, assuming phase discrimination is possible. Early PTV methods involved tracking particles through four or more consecutive images [14, 21] and regularly employed schemes for the minimization of trajectory length and angular deviation. While comparatively robust, the

tracking yield of these methods was low in comparison to the number of possible measurements. Also proposed was the binary image cross-correlation [34, 40]. For this method, a windowed cross-correlation, centered on each particle, was performed between the two images which provided a displacement estimate. Another two-frame PTV method proposed the use of a heuristic match probability to determine the most probable trajectories [5]. This two-frame method was found to be an improvement over the traditional four-frame methods in terms of computation expense, tracking yield and allowable dynamic ratio. Similar to the heuristic match method, a 'fuzzy logic' PTV algorithm has also been proposed [35]. It is important to note that all previously mentioned PTV methods rely on a 'smoothness parameter', indicating *a priori* knowledge of the flowfield which is not always available for MPFs.

Several methods utilize an initial PIV analysis of the flowfield to provide a 'first guess' for the particle trajectories [10, 17]. These methods, often referred to as 'super-resolution PIV' or 'hybrid PIV/PTV', showed significant increases in the tracking yield and dynamic range for densely seeded flows. Other super-resolution methods have been presented which utilize improved particle-matching techniques, such as Kalman filtering [32] and an improved global interpolation scheme [10]. The previously described match probability method [5] has also been presented as a hybrid scheme [20] which showed improvements in vector yield. However, it should be emphasized that these methods would be unable to track particles that do not behave as flow tracers, owing to their heavy reliance on PIV-derived predictions of the particle velocities.

Several two-frame PTV algorithms have been presented that do not rely on a PIV-derived velocity estimate. The relaxation algorithm [27] is an improvement over the original relaxation (ORX) method [26] for both the tracking algorithm and particle identification scheme. An iterative variational approach [31] was also proposed which makes use of a local regularization of the estimated particle trajectories to progressively improve the tracking efficiency. While effective, the algorithm required a large number of iterations (over 700) for a single image pair before a suitable convergence was achieved which significantly increases the computational cost of this method. A recent PTV method, referred to as enhanced particle tracking velocimetry (EPTV) [23], was shown to improve tracking reliability by utilizing the measured particle intensity information in combination to the particle position proximity, as two parameters of enhanced particle pair matching. The incorporation of particle-related information helped increase tracking efficiency significantly. Although this method appears to outperform all previously reported PTV methods, little attention was given on quantifying the actual error of the velocity measurements.

In a related class of works, image preprocessing was used for segregating discrete MPFs prior to PIV/PTV analysis. Kiger and Pan used a two-dimensional median filter [19], Khalitov and Longmire employed phase-discrimination by size and measured object intensity [18] and Cheng *et al* [9] expanded on this work by improving the image processing

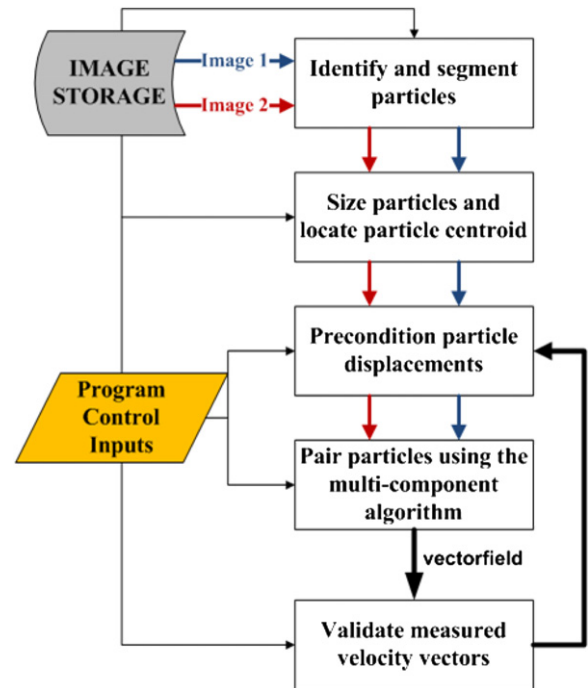


Figure 1. Flowchart illustrating the individual processes of the MP3-PTV algorithm.

algorithms for increasing the phase-separation accuracy, and in all cases the velocity fields for each phase were independently evaluated.

The objective of this paper is to introduce a new PTV algorithm that is aimed toward enhancing the capability for resolving MPFs and in particular situations under which the disperse phase does not follow the carrying flow and/or it cannot be efficiently separated from the carrying phase. We provide detailed error analysis and method validation using benchmark data and actual experimental measurements, in order to demonstrate the method advantages and possible limitations. The improvements of the method consist of a new and more robust particle segmentation procedure and an augmented multi-parameter particle-pairing approach incorporating particle image sizing methodologies [7]. We show that the combination of particle position, size and intensity within the particle-pairing process results in significant performance improvements when compared to previously reported results.

2. Particle tracking methodology

The PTV implementation presented herein, named multi-parametric particle pairing (MP3-PTV), is designed for use with single-exposure images. As illustrated in figure 1, the MP3-PTV algorithm requires the following steps: image pre-processing, particle identification, particle sizing, displacement preconditioning, particle pairing and validation of velocity measurements. With modification, the methods described could also be implemented for multi-exposed images or tracking with more than two frames. However, these were not explored herein.

2.1. Multi-parameter particle pair matching

For the MP3-PTV, three particle-related parameters are estimated and used for the pair matching: particle diameter (d), maximum ‘true’ intensity (I) and distance from the estimated particle position representing the ‘nearest neighborhood’ (NN). For each particle in frame one, a matching coefficient (C_{12}) is computed in association to each particle located in frame two, bounded within a user-defined search radius, r_s , centered on the particle’s estimated location in frame two, as shown in the following equation:

$$C_{12} = \left[W_d \left(\frac{|d_1 - d_2|}{d_{\max} - d_{\min}} \right) + W_I \left(\frac{|I_1 - I_2|}{I_{\max} - I_{\min}} \right) + W_{\text{NN}} \left(\frac{\text{NN}}{r_s} \right) \right] / (W_d + W_I + W_{\text{NN}}). \quad (1)$$

The difference in each matching parameter (d , I and NN) is normalized by its maximum possible value between frame one and frame two. A set of variable weighting factors, W_d , W_I and W_{NN} , are placed on each pair-matching parameter. In doing so, the relative emphasis on each parameter can be adjusted to match the image properties. For example, it would be prudent to decrease W_d for a monodisperse particle size distribution as the particle diameter will provide limited information for pair matching. The opposite would be true when dealing with a broad distribution of particle sizes. For images with abrupt spatial variations in laser intensity, W_I should be decreased. Setting W_d and W_I to zero reduces the pair matching to a simple nearest-neighbor (NN) algorithm. When operating as a NN algorithm with displacement preconditioning, the search radius is set to the theoretical optimal value of $\sqrt{\pi} \times d_t$, as defined by Keane *et al* [17], where d_t is the imaged particle diameter. Lastly, the matching coefficient is normalized by the sum of the weighting factors. This normalization assures a value of C_{12} between zero and one, where zero indicates a perfect match and a value of one implies the worst possible match.

Once computed for all possible particle pairs, the matching coefficients are arranged in ascending order. Pair matching begins with the lowest value of C_{12} and continues until the maximum number of measurable matches is met or the number of possible matches has been exhausted. The maximum number of measurable matches between a given frame pair is equal to the number of particles in either frame one or frame two, depending on which is the lesser value. As each particle in frame two is matched, it is removed from all possible matches with other particles in frame one thus assuring that each particle pairing is unique.

2.2. Particle identification and segmentation

2.2.1. Previous particle identification methods. The simplest and most commonly utilized method for particle identification is the single-value threshold (SVT) binarization. The SVT groups adjacent pixels in the images into a particle, provided the pixel intensity value is above a global threshold level. This method is fast and easy to implement. SVT, however, has serious limitations, notably an inability to cope with overlapped particles and uneven image illumination.

Locally varying threshold values, referred to as multiple threshold binarization, can be used to partially correct uneven illumination. This method does not, however, adequately address overlapped particles within the flowfield which is a vital aspect when dealing with simultaneously seeded MPFs and at high seeding densities.

The dynamic threshold binarization (DTB) detection method [27] is an improvement over the single and multiple threshold binarization. The algorithm efficiently handles uneven illumination and overlapped particles by locally adjusting the threshold value of each particle until the mean intensity level (gray level) is less than a preset contrast level. While an enhancement over other binarization methods, the DTB often truncates the particle image which has implications with regard to particle sizing. A modification to this method has also been proposed [23] that utilizes the maximum particle intensity level instead of the mean for comparison with the preset contrast level. However, we have found this method not to perform robustly when discriminating and separating overlapping particles.

Another particle segmentation technique is the particle-mask correlation [33]. For this method, a cross-correlation of a generic two-dimensional particle profile is performed for all pixels with subareas of high correlation taken as identified particles. This method effectively separates overlapped particles as well as handling uneven illuminations; however, it is sensitive to image noise, which can sometimes lead to false particle identifications [27].

2.2.2. Erosion/dilation thresholding. A method, which we term here as erosion/dilation thresholding (EDT), is proposed for particle identification and segmentation. The EDT is based on two commonly utilized morphological operations related to image processing: erosion and dilation. In the field of mathematical morphology, the intensity profile of a two-dimensional grayscale image is often referred to as an ‘elevation’ above the image plane. Using the elevation analogy, an efficient peak-finding routine can be achieved by protecting the local maxima (peaks) while simultaneously eroding the remaining ‘landscape’ until only the peaks remain, as illustrated in figure 2. For the EDT, this erosion is accomplished by a variable structuring element (SE) which is iteratively subtracted from the image intensity distribution at each step. The SE size is equal to the image size (shown in figure 2) and is assigned initial value (global) of one.

For each erosion step, adjacent pixels are grouped together, so long as they are within an 8-pixel neighborhood. An 8-pixel neighborhood stipulates that pixels are ‘neighbors’ when they share a common edge or vertex (i.e. pixels situated orthogonally or diagonally). For two-dimensional images, the 8-pixel neighborhood is considered to be superior to the 4-pixel neighborhood, thus its choice for the EDT algorithm. Each pixel group (neighborhood) is then assigned a particle ID number (p_{num}) and the local peak of each group is identified and shielded from erosion by setting the SE value to zero at that location. The SE is also set to a value of zero at all pixel locations where $I_{xy} = 0$ and then subtracted from the image. The process of grouping pixels, adjusting the SE, and

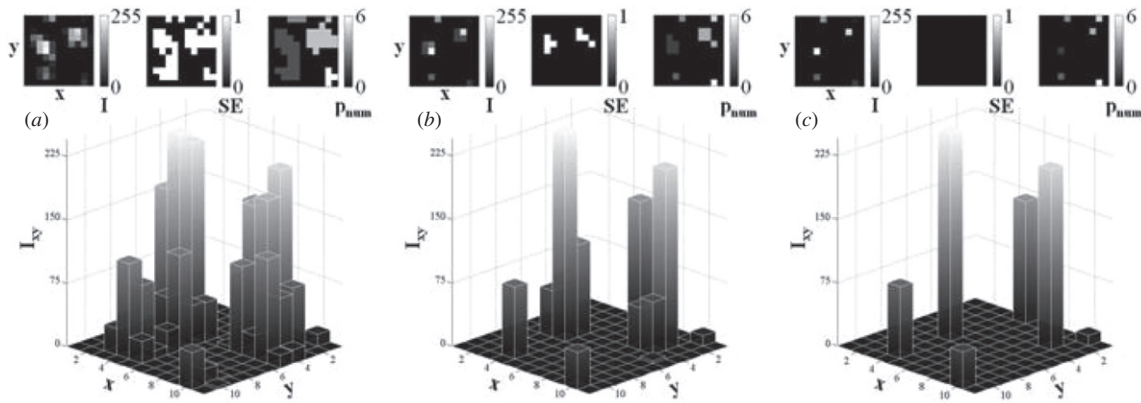


Figure 2. Selected erosion steps of (starting upper left, clockwise) an 11×11 pixel image with six particles, the SE and grouped pixels for an 8×8 neighborhood; selections correspond to erosion step (a) 1, (b) 110 and (c) 232 (final).

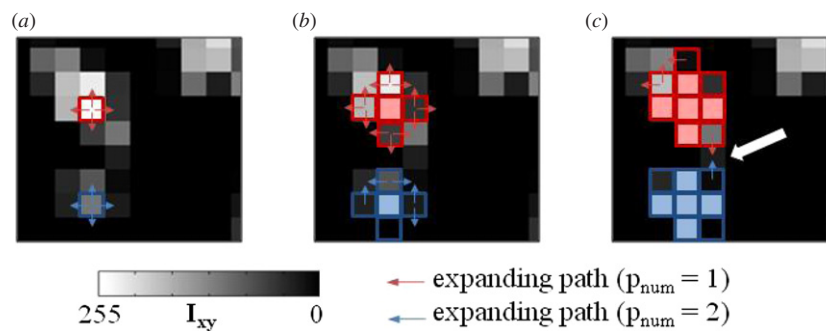


Figure 3. Illustration of the iterative dilation of two identified peaks (red and blue) for (a) step one, (b) step two and (c) step three.

subtracting the SE from the image is repeated (see figure 2) until all SE values equal zero or the number of erosion steps is equal to the maximum image intensity.

Additionally, the global value of the SE may be greater than one. For a global SE value of one, the number of erosion steps required to identify all particle peaks is equal to the maximum image intensity (256 for an 8 bit grayscale image). Increasing the global SE value beyond a value of one reduces the number of required erosions steps and, therefore, the computational requirement. Maintaining a value of one, however, assures that all local peaks will be identified.

After the image erosion, an iterative dilation of the original image and identified peaks (figure 2(c)) is performed in which pixels adjacent to the identified peaks are assigned the same p_{num} , thereby identifying the adjacent pixels as part of the same particle. The dilation of each identified peak, illustrated in figure 3, is based upon the following rules:

- (1) Expansion can only occur in the four principle directions (up, down, left, right) and only if the intensity of the expanded pixel (I_{exp}) is above a user-defined base level.
- (2) Expansion of each pixel can only extend by one adjacent pixel per dilation step.
- (3) Pixels previously assigned to a particle cannot be reassigned by expansion of another adjacent particle.
- (4) The computed intensity ratio for each pixel expansion, defined as the intensity of the source pixel (I_s) divided by I_{exp} , is less than one.

- (5) For particle expansion conflicts (white arrow in figure 3(c)), the source pixel with the highest intensity (I_s) will claim the expanded pixel.

Rules 1–3 allow for a controlled expansion of each peak. Rule 4 prevents an expanding particle from claiming unassigned pixels belonging to an adjacent particle. Particle dilation then continues iteratively until the intensity value of all adjacent pixels falls below the user defined base level, or minimum intensity level for particle dilation. This process ensures maximum information is made available for subsequent use with the particle sizing algorithms.

2.3. Particle sizing

Six previously presented digital particle image-sizing methodologies (DPIS) were assessed within the current study. Two of the methods are classical implementations for sizing particle images: intensity weighted centroid (IWC) and three-point Gaussian (TPG) [22]. The four remaining methods are recent implementations that have been shown to reduce the errors associated with DPIS [7]. A short discussion of each method is provided below for completeness. For details and further clarification of these sizing methods, the reader is directed to the work by Brady *et al* [7].

2.3.1. Intensity weighted centroid and pixel counting. Both the IWC and pixel counting are fast and easy to implement methods for computing the centroid and diameter, respectively,

of an imaged particle. While robust, their measurement accuracy has been shown to be sensitive to the image quality and overly aggressive thresholding can compromise their effectiveness. This issue can be particularly problematic when the SVT identification method is used, since aggressive thresholding is required in order to separate overlapped particles.

2.3.2. Discrete Gaussian methods. From optical theory, it is accepted that the distribution of reflected light for particles imaged by a coherent light source is described by an Airy point spread function [2]. The TPG fitting scheme makes use of this approximation by fitting a one- or two-dimensional Gaussian curve to the maximum intensity pixel and four adjacent pixels [22]. As with the IWC, the TPG method is fast and easy to implement. It performs poorly, however, when applied to large particle images and over-saturated particles, both of which are common when dealing with simultaneously seeded MPFs.

The four-point Gaussian (FPG) is a two-dimensional fitting scheme developed by Brady *et al* [7] to overcome limitations with the traditional TPG method, specifically the inability to deal with saturated particle images. This improvement is accomplished through a pixel selection routine that selects only unsaturated pixels. Additionally, the pixel selection for the FPG is governed by a set of rules that ensures the solution is non-trivial. The FPG is still limited given that it only utilizes a total of four pixels for particle centroid and diameter measurement.

Brady *et al* [7] also presented a least-squares Gaussian (LSG) fitting scheme that utilized all available pixels for the measurement of particle centroid and diameter. Least-squares minimization methods are regularly used for solving overdetermined systems, which correctly describes the fitting of a Gaussian distribution to a noisy particle image. Performance of the LSG method is superior to other least-squares fitting schemes [22] given that it utilizes the maximum amount of information available in the particle image.

2.3.3. Continuous Gaussian methods. Pixel intensity discretization also contributes to error associated with particle sizing. The previously described sizing methods assume that the measured intensity value at each pixel center is equal to the true intensity reported. In reality, the measured intensity value is equal to the intensity value integrated over the pixel area plus the sensor noise. This difference between measured and true intensity introduces significant errors with regard to particle centroid and size estimation. A continuous four-point Gaussian (CFPG) and continuous least-squares Gaussian (CLSG) fitting schemes [7] are an improvement over the previously described FPG and LSG methods as they compare the integrated intensity value at each pixel location to the measured value. In doing so, the methods compute the ‘true’ intensity value at each pixel location. This is of particular importance for this study given that the MP3-PTV uses particle intensity as a particle-matching parameter.

The work by Brady *et al* [7] was focused on determining the accuracy of these methods for particle sizing only and their utility for velocimetry applications was not explored

in detail. Therefore, for completeness, the dependence of the MP3-PTV accuracy to the choice of particle position and diameter estimation method was considered herein.

2.4. Inter-frame displacement preconditioning

Providing an estimate of the particle displacement increases the likelihood of correctly matching particles between frames, especially for high particle densities. The MP3-PTV method shown here considered three methods for displacement preconditioning, as described below.

2.4.1. Hybrid PTV-PIV. Previous researchers have shown that the use of a PIV-derived estimate of particle displacement greatly increases the allowable measurement density for PTV [10, 17]. Following this methodology, a PIV analysis was performed on the flowfield prior to pair matching. The accuracy of the PIV analysis is, therefore, very important given that an invalid measurement will cascade into multiple errors during particle pairing. For the work presented here, PIV processing of the images was carried out, prior to particle identification/sizing/tracking, using the robust phase correlation (RPC) [11, 12]. Once the PIV velocity field has been computed, an interpolation is required to provide a displacement estimate for each individual particle, given that the PIV-derived velocity estimates are uniformly spaced and the particle centroid locations are randomly distributed. A cubic-spline interpolation, using the built-in MATLAB function ‘interp2’, was performed for each particle centroid, resulting in a PIV-estimated particle velocity at that location. This velocity estimate, along with the inter-frame time, provided a displacement estimate for each particle.

2.4.2. PTV preconditioning using previous particle tracking velocity estimation. The particle velocity distribution, as measured by PTV from a previous image pair, was also utilized as a displacement estimate. It is important to note that utilizing the previously measured particle velocities assumes that the flowfield is temporally resolved.

Since the particle velocities measured by PTV are irregularly distributed, a distance-weighted average was employed for the neighboring particle velocities, measured from the previous image pair, to provide a displacement estimate for each particle in the current image. Within a user-defined search radius (r_S), the PTV-derived velocities were weighted with a radially symmetric Gaussian distribution, $A(r)$, centered on the location of the particle centroid in the current image. The standard deviation of the Gaussian was set such that the value of the function at r_S matched the user-defined value. Calculation of the particle velocity estimates, u_i and v_i , are shown in equation (2). This calculation was performed for each particle in the current image, thereby

providing a PTV-derived displacement estimate from the previous image pair:

$$\begin{aligned}
 A(r) &= e^{-r^2/2\sigma^2} \\
 \sigma &= \sqrt{-\langle r_s^2 \rangle / (2 \ln [A(r_s)])} \\
 u_i &= \sum A(r) \times u(x, y) / \sum A(r) \\
 v_i &= \sum A(r) \times v(x, y) / \sum A(r).
 \end{aligned}
 \quad (2)$$

2.4.3. PTV with no displacement preconditioning. The presented MP3-PTV algorithm also has the capability to operate without any estimation of particle displacement. This is appropriate when dealing with particle motion that does not locally correlate with the motion of adjacent particles (i.e. random trajectories).

2.5. Outlier detection and validation

Flowfield measurement by PIV and PTV typically requires a data validation step where each velocity vector is labeled as either valid or invalid and removed/replaced if necessary. Numerous studies have sought to address the validation of planar PIV data [25, 30, 36, 38]. The MP3-PTV algorithm makes use of two validation methods, one based on the deviation of each measurement from the local population, which is suitable for a single-phase flow, and one utilizing the pair-matching coefficient (C_{12}), which is suitable for both single and MPFs. It is important to note that, for the MP3-PTV, only flagging and removal of spurious vectors is performed.

Statistically comparing each vector to its surrounding velocities is a common method for detecting erroneous measurements for PIV. The MP3-PTV employs the universal outlier detector (UOD) method [36, 38] which compares the median deviation of the measured vector to the median absolute deviation (MAD) of the surrounding vectors as defined by the search radius, r_s . Once an outlier has been detected, the displacement estimate (preconditioning) is updated using the median value of the local population. The pair-matching and validation steps repeat iteratively until all prescribed validation steps are completed. As stated previously, the UOD assumes that the particle trajectories are driven primarily by the flow and, therefore, is most suitable for single-phase flows and multiphase particles that trace the flow relatively well. Special care should be made when applying the UOD to MPFs where the Stokes number of the particles is in the vicinity of or greater than a value of one.

Validation was also performed using the matching coefficient, C_{12} , as a low-pass filter. C_{12} is an ideal parameter for validation of MPFs, given that it varies from a value of zero (perfect match) to one (worst match) and represents how well the two particles comprising each velocity measurement match each other with respect to size, intensity and estimated displacement. An appropriate threshold value for C_{12} can be made through observations of either a single tracking step or the ensemble-averaged results over multiple steps. For example, selecting a C_{12} threshold of 0.2 would thereby disregard all velocity measurements where the pair-matching coefficient (C_{12}) was greater than a value of 0.2.

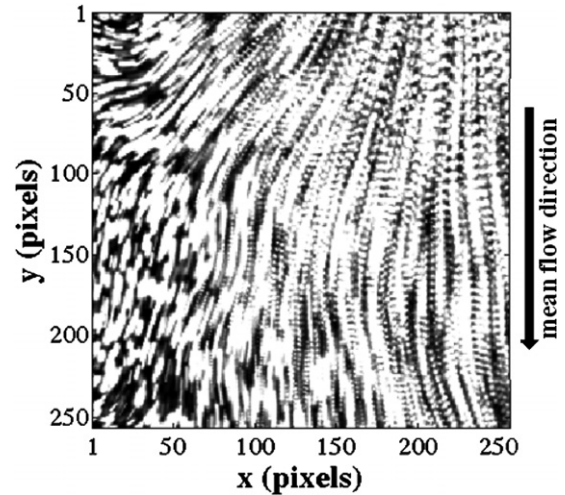


Figure 4. Flowfield visualization created by overlapping images 1–10 of the VSJ#301.

Table 1. Image properties for VSJ#301.

VSJ#301		Units
Image size	256 × 256	pixels
Imaged area	4 × 4	cm
Laser thickness	2	mm
Inter-frame time	0.005	s
Max velocity (in-plane)	10	pixel/interval
Max velocity (through-plane)	1.5	pixel/interval
Particle diameter	~5	pixels

3. Results

3.1. Benchmarking against previous PTV algorithms

Images provided by the PIV-STD Project were chosen to initially test the MP3-PTV. The PIV-STD Project, supplied by the Visualization Society of Japan (VSJ) [28, 29], provides simulated PIV image sets for the evaluation and testing of different processing algorithms. This section describes the selected VSJ image set as well as the testing and subsequent performance of the MP3-PTV when employed as a conventional algorithm on a single-phase turbulent flowfield.

3.1.1. Visualization society of Japan standard images. The specific set chosen for evaluation in this study was VSJ#301: transient three-dimensional jet shear flow. This image set has been used by other researchers for the development of PTV algorithms [14, 23, 26, 27, 31, 40]. Figure 4 shows ten overlapped images from the VSJ#301 to illustrate the particle trajectories. A summary of the image parameters used to generate the VSJ#301 are shown in table 1.

3.1.2. Results for the VSJ#301. The following subsections provide results of an error analysis regarding the different identification, sizing and tracking modes of the MP3-PTV as applied to the VSJ#301. In addition to calculating measurement yield and reliability, the particle velocity error was also quantified. All presented results were averaged

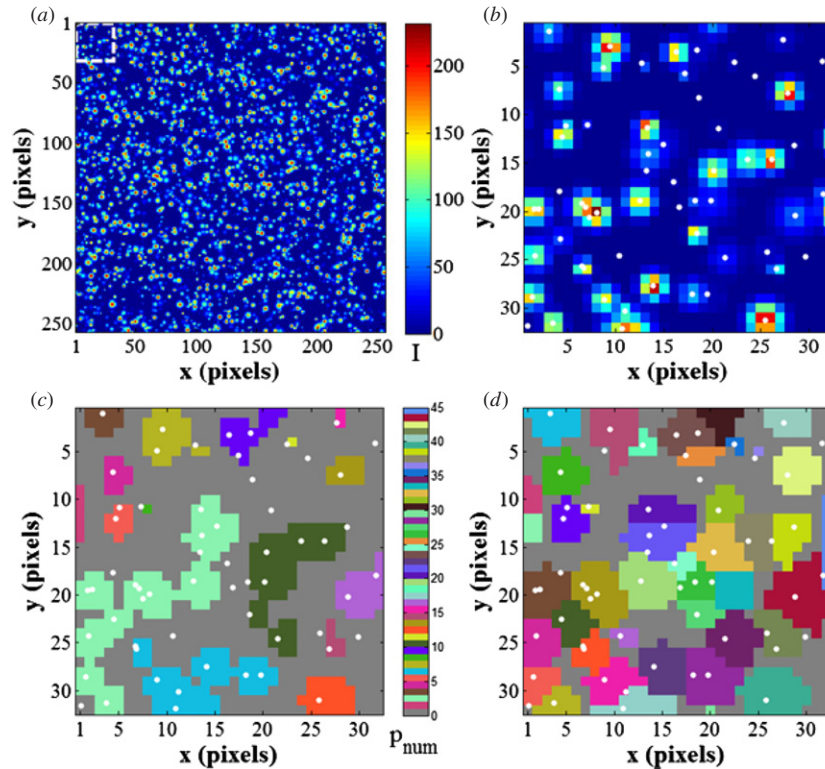


Figure 5. Segmentation of IM1 of the VSJ#301: (a) original image, (b) cropped region with known particle locations marked with white dots, (c) SVT segmented particles with $I_{th} = 10$ and (d) EDT segmented particles with $I_{th} = 0$.

over ten images of the VSJ#301, contributing over 22 000 measurable particles to the mean statistics.

Particle identification Recalling figure 1, the first task is to locate and segment the individual particle images. When using the SVT, the initial image thresholding (I_{th}) was varied from 1 to 100 to determine the most efficient level for separating overlapped particles, which was $I_{th} = 50$ counts. This ‘optimal’ thresholding level was chosen as it resulted in the maximum number of identified particles independently identified within a single image. It is important to note that the EDT does not require trial and error to determine an ‘optimal’ initial thresholding value. Given that the VJS#301 images were simulated without noise, an initial image thresholding was not applied when using the EDT. Figure 5 illustrates the typical results of the particle identification step using both the SVT and EDT algorithms for a cropped region of frame one.

Comparing figures 5(c) (SVT) and 5(d) (EDT), the superior ability of the EDT to separate overlapped particles versus the SVT, the most basic form of particle identification, is readily apparent. In addition to separation of particles, the EDT preserved more of the particle information as it did not require high threshold levels for particle separation, as did the SVT. For the EDT, the number of identified particles for the first two frames was 2111 and 2099, respectively. Other, more advanced, particle identification methods have been employed on the VSJ #301 such as the previously described particle mask correlation (PMC) [33], DTB [27] and the modified dynamic threshold binarization (MDTB) [23]. The number of identified particle by EDT (2111) was either greater or equivalent to

the value reported for the PMC (1134), DTB (1269/2338) depending on two different initial thresholding values, and the MDTB (2034).

The actual number of identifiable particles in each image was also estimated assuming that a particle will occlude an adjacent particle located within one-half of its diameter. While this methodology ignores the apparent diameter of the particles, resulting from the Gaussian laser sheet profile, it does provide a quantitative estimate of the number of identifiable particles in a particular VSJ#301 image. Following this method for the first VSJ#301 image, the number of identifiable particles is approximately 2200 out of the 4000 available, compared to 2111 identified particles using the EDT. From this result and comparisons to the literature, it was concluded that the sufficiently high number of particles have been extracted from each image using the EDT.

Particle sizing The number of sized particles returned by each method, described in section 2.3, is given in figure 6. Also illustrated in figure 6 are the maximum number of identifiable particles as well as the number of particles identified by the EDT (n_I) and the MDTB by Mikheev and Zubtsov [23]. The number of identified particles will equal the number of sized particles (n_S) if the sizing method never fails, as is the case with the IWC. All other sizing methods are subject to constraints which can preclude them from successfully sizing all identified particles. After the IWC, the LSG and CLSG sizing methods performed best, particularly when coupled with the EDT. Using the SVT in conjunction with the Gaussian sizing methods resulted in a dramatic drop in the number

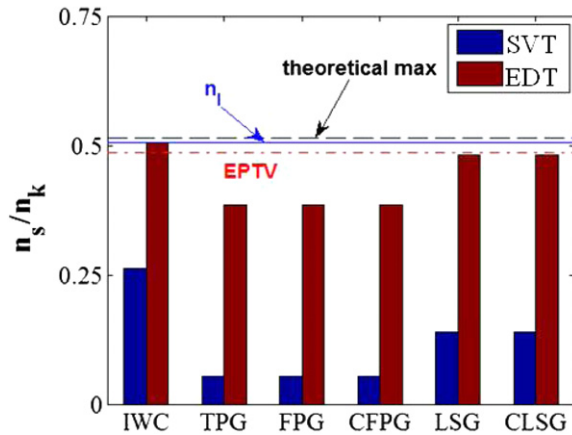


Figure 6. Performance comparison of the different particle identification and sizing methods.

of sized particles versus the IWC. This drop resulted from the aggressive thresholding that cropped the particle images considerably.

Figure 7(a), showing the particle size distributions for all methods, illustrates the enhanced performance of the EDT identification and LSG/CLSG sizing methods. The IWC showed a measurement diameter bias of ~ 1.5 pixels as compared to the other methods for the EDT, which was not unexpected given the previously published performance of the IWC. The measured diameter distribution reported for EPTV [23] is also shown in figure 7(a). Severe peak locking was observed when using the SVT, especially with the IWC, TPG, FPG and CFPG sizing methods. Overall, the size distributions for the measured particles found by LSG and CLSG were somewhat insensitive to the particle identification method.

The EDT also provided a more accurate measurement of the particle centroid than the SVT, as shown in figure 7(b) and table 2. The position error, e_{xy} , of the IWC sizing method was the most sensitive to the particle identification method, as evidenced by the $2\times$ decrease in e_{xy} between the SVT and EDT. A decrease in e_{xy} was observed for all sizing methods when utilizing the EDT, a result of the increased available particle information and lower incidence of overlapping. The position error in relation to the subpixel location of the known

Table 2. Average position error and measured peak intensity error for VSJ#301 (acronyms defined in the nomenclature).

		e_{xy} (pixel)	e_I (counts)	$e_{RMS,xy}$	$e_{RMS,I}$
SVT	IWC	0.40	-22.3	0.46	43.1
	TPG	0.15	-13.9	0.21	13.1
	FPG	0.15	-12.6	0.20	14.5
	CFPG	0.15	-6.7	0.20	16.4
	LSG	0.10	-11.3	0.16	14.5
	CLSG	0.10	3.6	0.17	16.7
EDT	IWC	0.21	-26.7	0.18	30.6
	TPG	0.12	-19.0	0.16	20.5
	FPG	0.13	-17.0	0.16	20.5
	CFPG	0.13	-6.2	0.16	22.0
	LSG	0.08	-16.3	0.12	21.3
	CLSG	0.08	0.2	0.12	18.0

particle is also shown in figure 7(c). Peak locking was again observed for the TPG, FPG and CFPG.

The error in measured maximum intensity, (e_I), is also shown in table 2. The intensity error was somewhat insensitive to the particle identification method, indicating that aggressive thresholding does not affect the measurement of maximum particle intensity. The continuous Gaussian sizing methods (CFPG and CLSG) exhibited the lowest e_I , owing to their unique treatment of the particle image.

The results of the previously described error analysis confirmed that the most accurate combination of particle identification and sizing methods was the EDT and CLSG, respectively. The remaining results of the VSJ#301, therefore, are presented utilizing these methods.

Particle-pairing effectiveness (velocity measurement) Similar to previous works [23, 27], quantification of particle-pairing effectiveness was evaluated through the total measurement yield, E_Y , and reliability, E_R , as shown in equation (3). The yield was defined as the ratio of measured particle trajectories (D) to the total number of known trajectories (V) while reliability was defined as the ratio of correctly identified (N) to the total number of measured particle trajectories (D):

$$\begin{aligned} E_Y &= D/V, & E_R &= N/D \\ E_F &= E_Y \times E_R. \end{aligned} \quad (3)$$

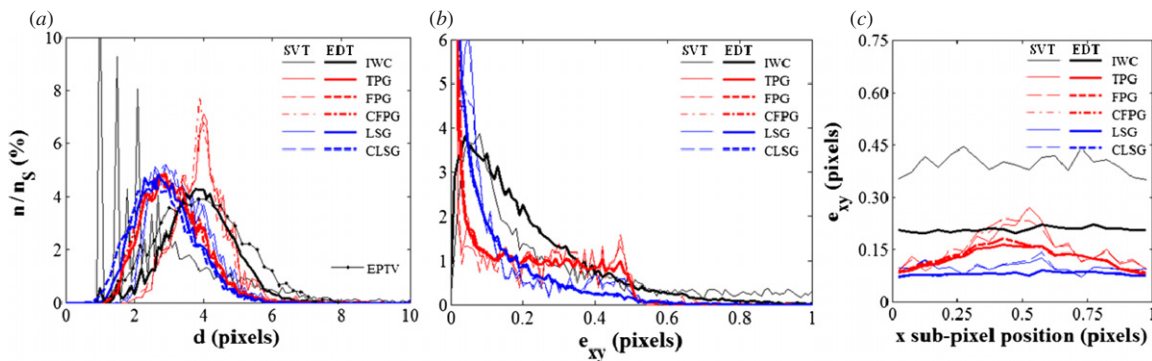


Figure 7. Comparison between the SVT and EDT VSJ#301 results for (a) measured particle size distributions, (b) histogram of position error and (c) position error versus subpixel particle position.

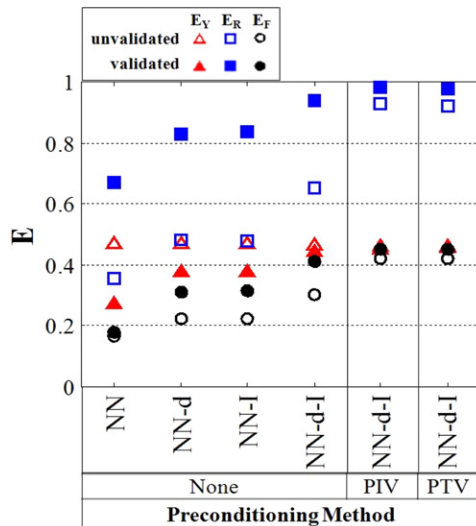


Figure 8. Performance of the MP3-PTV algorithm for the VSJ#301 images.

Also introduced was a new cumulative metric, measurement efficiency (E_F), which was defined as the product of the yield and reliability.

Initially, pairing was completed with no displacement preconditioning, the results of which are shown in figure 8, to evaluate the MP3-PTV without *a priori* knowledge of the flowfield. A uniform weighting of the pair-matching parameters ($W_{NN} = W_d = W_I = 1$) was utilized along with a second window search radius of 10 pixels, which was greater than the max given displacement for the image pairs. The x -axis labels denote the combination of the particle-pairing criteria used as shown in equation (1): NN: nearest neighborhood, d : diameter, I : intensity.

Without validation (figure 8, empty symbols), the vector yield, E_Y , was uniform across all cases, an expected result since E_Y is a function of the number of identified trajectories. With intermediate validation (figure 8, solid symbols), both E_Y and E_R increased as additional matching parameters were added. For all pair-matching methods, E_Y was lower with validation than without, but this decrease was small for the three-component method. The vector reliability, E_R , was considerably higher with validation than without, with levels approaching 95% for the three-parameter method (NN- d - I). Taking into account both yield and reliability, the vector efficiency, E_F , of the three-parameter method was $\sim 42\%$. This result was considerable, given that no displacement preconditioning was provided and the maximum theoretical efficiency was $\sim 50\%$, based on the number of identifiable particles in each image.

The effect of displacement preconditioning was also investigated using PIV and previous PTV. Processing parameters for the PIV displacement preconditioning are shown in table 3. Only results for the NN- d - I pair-matching method with preconditioning are shown in figure 8, both with and without intermediate validation. Applying a displacement estimate increased E_R by $\sim 54\%$ over the results with no preconditioning. When employing intermediate validation,

Table 3. PIV displacement preconditioning properties for VSJ#301.

VSJ#301		Units
Number of correlation passes	2	#
Window size	$64 \times 64, 32 \times 32$	pixels
Windowing function (zero padded)	Gaussian	
Grid resolution	8×8	pixels
Number of validation passes	2	#

the increase in E_R was smaller as compared to the unvalidated result. Given that the unvalidated E_R was nearly a value of one, the disproportionately small increase in E_R was understood to be a function of the upper limit of vector reliability for the VSJ#301. No appreciable sensitivity was observed for the different preconditioning methods, indicating a uniform quality between the PIV and PTV displacement estimates. More importantly however, the validated MP3-PTV with NN- d - I shows nearly the same overall efficiency (42%) compared to the analysis with preconditioning (45%). This suggests that the proposed algorithm performs equivalently to the super-resolution hybrid approach yet without requiring initial velocity estimation. This is a powerful attribute for resolving particle motion that does not follow the flow.

Comparisons with published results of other PTV algorithms for the VSJ#301 are shown in table 4. All published results were taken from the corresponding publications. The methods included in the comparison are four-frame inline tracking (FIT) [14], binary cross-correlation (BCC) [40], ORX method [26], new relaxation (NRX) method [27], variation tracking (VAR) [31] and EPTV [23]. It should be noted that all these methods employ different validation or preconditioning procedures.

Without displacement preconditioning or validation (¹), the MP3-PTV algorithm outperforms all other methods except for EPTV, when comparing the overall performance using vector efficiency, E_F , although E_R is less, this is compensated by a significant increase in E_Y . Employing intermediate validation (²), the MP3-PTV vector reliability, E_R , was now comparable with other methods and the E_F was 41.5% only marginally less than the EPTV method. Utilizing displacement preconditioning (³) and intermediate validation (⁴) further improved the performance of the MP3-PTV algorithm in comparison to other algorithms, resulting in the best overall efficiency of 45%. Errors in the velocity measurements were approximately equal to the previously reported position error, e_{xy} as it is determined by the accuracy of the subpixel estimation method. It was concluded that the main source of velocity error resulted from the measurement of the particle location. The previous works listed did not report errors for their velocity estimation so no direct comparisons were possible.

3.2. Benchmarking of MP3-PTV for multiphase flows

A simulated data set was generated using an in-house algorithm to replicate a MPF having a bi-modal distribution of diameters. The MPF image generation was designed to replicate the imaging conditions of a MPF experiment

Table 4. Comparison of published results for the #301 VJS image set (D = number of measured vectors, N = number of correct vectors and V = number of known vectors).

	D	N	V	E_Y (%)	E_R (%)	E_F (%)	e_{uv} (pixel)	$e_{RMS,uv}$
FIT ^a	779	671	4042	19.3	86.1	16.6		
FIT ^b	630	559	4042	15.6	88.7	13.8		
BCC	860	788	4042	21.3	91.6	19.5		
ORX	786	762	4042	19.4	96.9	18.9		
NRX	808	788	4042	20.0	97.5	19.5		
VAR	872	865	4042	21.6	99.2	21.4		
EPTV	1759	1733	4042	43.5	98.5	42.9		
NN- $d-I^1$	1880	1227	4042	46.5	65.3	30.4	0.08	0.13
NN- $d-I^2$	1783	1676	4042	44.1	94.0	41.5	0.09	0.14
NN- $d-I^3$	1831	1701	4042	45.3	92.9	42.1	0.09	0.14
NN- $d-I^4$	1855	1822	4042	45.9	98.2	45.1	0.09	0.13

^aSearch radius of 0.2 pixel.

^bSearch radius of 0.1 pixel.

¹No intermediate validation.

²Four passes of validation.

³Same as ¹ with PIV preconditioning.

⁴Same as ² with PIV preconditioning.

conducted by the authors and which will be presented in section 3.3. The current section of the paper provides information regarding the generation of the MPF image set and subsequent performance of the MP3-PTV when employed on a simultaneously seeded multiphase turbulent flowfield. For the MPF image set, all reported values were averaged over 100 individual images, which ensured statistical convergence was achieved.

3.2.1. Generation of the MPF images. The MPF image set was generated based on the results of the rib-channel MPF experiment (see section 3.3.1). The experimental particle concentration and diameter distribution were utilized as inputs for generating each set of images. Particle identification and sizing were performed on the experimental images with both tracer particles and sand particles only using the EDT and CLSG. For each identified particle in the experimental image, an identically sized particle was generated and randomly placed within the corresponding simulated image with no constraints to keep individual particles separate from one other.

For each particle, the Fraunhofer diffraction pattern was represented by a Gaussian distribution, a common approximation when generating PIV images: the particle images include contributions from their diameter and relative distance to the focal plane center as well as effects related to the diffraction limited resolution of the camera/lens arrangement. This model, however, does not account for the interference of particle images produced from the complex wavefunction. To properly address this issue, the particle images were generated using the integrated form of the Gaussian intensity profile, as shown in the following equation:

$$\begin{aligned}
 I(x, y) &= I_0 \frac{\pi d_p^2}{32} [\operatorname{erf}(\alpha) - \operatorname{erf}(\alpha) \cdot \operatorname{erf}(\beta) - \operatorname{erf}(\beta)] \\
 \alpha &= \sqrt{8} (x - x_i - 0.5)/d_p \\
 \beta &= \sqrt{8} (y - y_i - 0.5)/d_p,
 \end{aligned} \tag{4}$$

where x_i and y_j denote the center particle location and I_0 represents the maximum pixel intensity. This integral form is a more precise representation of the digital recording process as the sensors record the integrated light intensity over the individual pixels.

Image noise was added using the built-in MATLAB function ‘imnoise’. This command added Gaussian noise with a prescribed mean and variance across the entire image. Gaussian noise was added to represent the thermal noise that is common in CCD and CMOS cameras. The level of noise added to the MPF images was varied until a suitable correspondence to the experimental image intensity histogram was found.

Simulated particle displacement was controlled separately for the flow tracers and sand particles. Displacement of flow tracers was described by a Rankine vortex centered at $x = 128$ and $y = 128$ pixels, having a radius of 10 pixels and maximum velocity of 10 pixels per framestep. A uniform horizontal velocity of $u = 5$ pixels per framestep was applied to sand particles along with a randomly distributed vertical velocity ranging from $v = \pm 5$ pixels per framestep, representing ballistic particle trajectories unaffected by the motions of the carrier flowfield. The simulated MPF and experimental MPF images are shown in figure 9, along with the MPF displacement velocity fields. The combined MPF image is also shown in figure 9.

To validate the MPF images, particle identification and sizing was performed using the EDT and CLSG. The measured size distribution of the MPF (not shown) matched closely with the size distribution of the original MPF experimental images for all simulated image types (flow tracer, sand and combined images).

3.2.2. Displacement preconditioning methods. Determining an appropriate particle displacement estimate for the MPF images is not straightforward given that two separate particle populations exist, each with their own relative motions. The

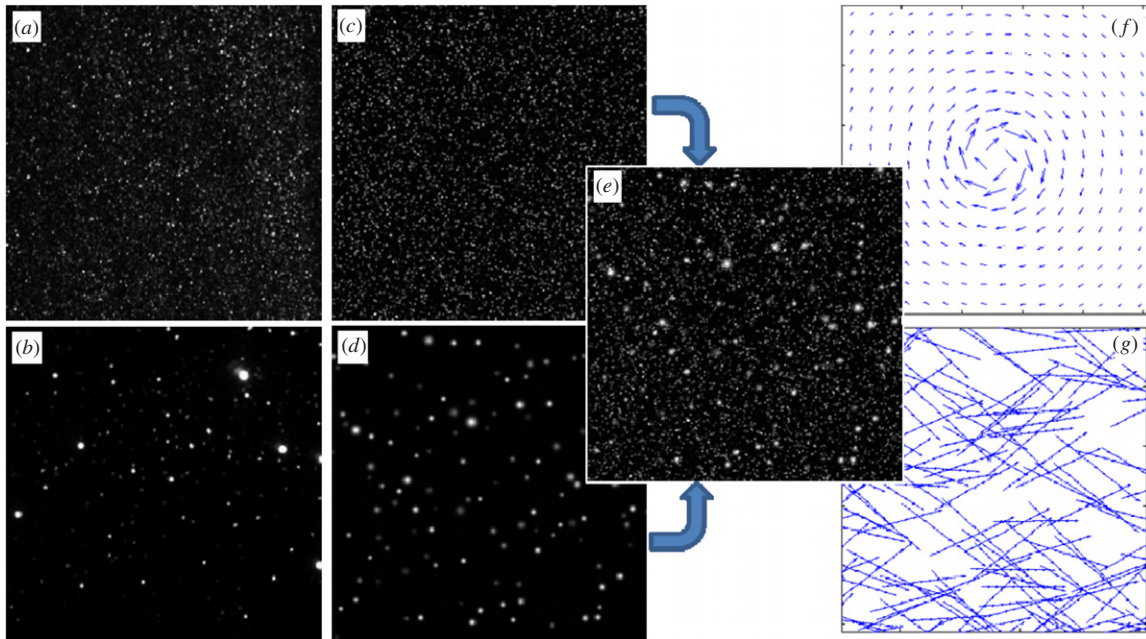


Figure 9. Sample experimental (a) tracer and (b) sand images with the corresponding simulated (MPF) images of (c) tracer, (d) sand and (e) combined along with the simulated displacements of (f) tracer and (g) sand particles.

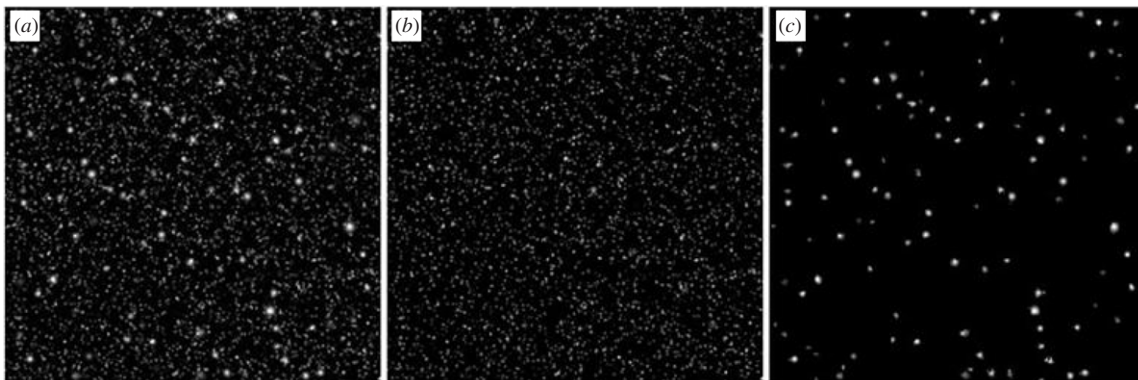


Figure 10. Results of the image segregation: (a) original MPF image, (b) separated flow tracers, (c) separated sand particles.

preconditioning method tested for this study was both based on a PIV correlation of the MPF images.

The measured particle size information was used to segregate each MPF image, which was then reconstructed into two separate image sets each having only flow tracers or sand particles. Previously utilized techniques for segregating simultaneously seeded discrete MPFs include median spatial filtering [19] and phase-discrimination by size and measured object intensity [18]. These methods, while effective, did not address the issue of overlapping particles. The results of MP3-PTV segregation process for a single image are shown in figure 10. Once separated, the flow tracers and sand particle images were processed independently using the RPC cross-correlation algorithm. This method provided a suitable displacement estimate for both particle populations, as shown figure 11. It is important to note that this method is limited to situations when a suitable particle-related parameter (diameter, intensity, shape) exists to segregate different populations.

3.2.3. Results for the in-house generated MPF set. A summary of the processing parameters utilized for the MPF image set is given in table 5. When the MPF images were segmented prior to computing a displacement estimate, an increase in vector reliability was observed for the MP3-PTV both with and without displacement preconditioning, as shown in figure 12. The vector validation step was omitted, given the dissimilar motions of the two particle populations. Overall vector efficiency for the multi-component algorithm (NN- $d-I$) with preconditioning was 49% and 46% for the flow tracers and sand, respectively. These values represented a 9% and 44% increase in measured vector efficiency for tracers and sand populations as compared to the NN PIV-hybrid tracking algorithm. It is also important to note that the measured vector reliability of the separated tracers was 98% for the multi-component algorithm with preconditioning, verifying that the detrimental feedback between the two populations had been successfully negated through the particle segmenting

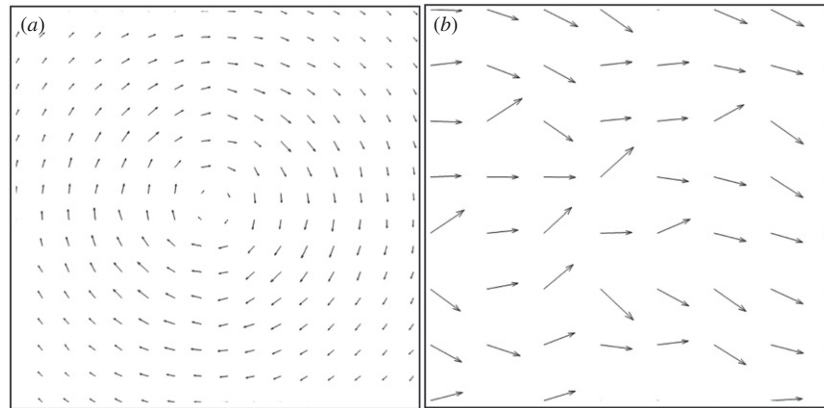


Figure 11. Displacement estimate using PIV between the first two MPF images without vector validation for (a) separated flow tracers and (b) separated sand particles.

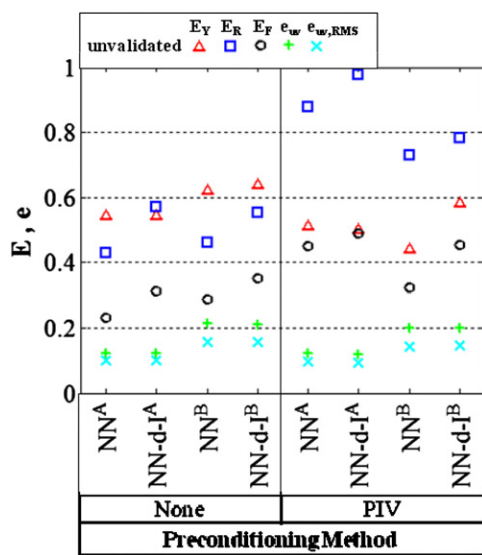


Figure 12. Performance of the MP3-PTV algorithm for the segmented MPF images, where ‘A’ and ‘B’ refer to the tracer and sand particles, respectively.

Table 5. MP3-PTV processing parameters for the MPF set.

MP3-PTV parameters (MPF set)	Units
ID and sizing method	EDT/CLSG
I_{th}	30 intensity
σ_s	4 #
W_d, W_i, W_{NN}	1/1/1 #
r_s (no preconditioning)	32 pixels
r_s (with preconditioning)	4 pixels
PTV validation	None

process. Separating the populations also served to decrease the diameter range of the tracer population ($d_{max}-d_{min}$). Recalling equation (1), decreasing the diameter range subsequently increases the effectiveness of the diameter pair-matching parameter as compared to the original image with both sand and tracer particles.

The measured velocity error for the tracers and sand particles was approximately 0.1 pixels/framestep and 0.2

pixels/framestep, respectively. As compared to the mean particle velocities, 2.2 pixels/framestep for the tracers and 8.1 pixels/framestep for the sand, this corresponded to a 4.5% and 2.5% error in measured velocity for the respective particle populations. The increased velocity error for the sand particles resulted from errors in the sand particle centroid estimation. This is an artifact of the segregation of sand particles overlapped with tracer particles, which sometimes resulted in irregular sand particle intensity profiles.

3.3. Experimental validation and testing

As referenced previously, a MPF experiment was conducted to provide a baseline for generating the MPF image set. A description of the experimental setup is detailed in this section as well as the performance of the MP3-PTV for experimental data. Results for a single-phase flowfield are presented first followed by results for a simultaneously seeded MPF. More details on the experiment and the analysis of the single flow results can be found in Cardwell *et al* [8].

3.3.1. Experimental setup. The MPF experiments were performed in a fully roughened channel having staggered rib arrays on two opposed walls. Flowfield measurements were achieved using an in-house developed time-resolved digital particle image velocimetry (TRDPIV) system and processing algorithm. An illustration of the test facility is shown in figure 13. The channel Reynolds number was 10k, based on the hydraulic diameter and bulk streamwise velocity. The entrance to the rib-roughened channel region, shown in figure 13, was chosen as the experimental measurement region.

A 20 W New Wave dual-head Pegasus laser was used to illuminate the flow, as shown in figure 13. Imaging normal to the laser sheet, a 1-megapixel Photron Ultima APX-RS high speed digital camera recorded images of the flow at 3000 fps, corresponding to a 1.5 kHz sampling rate. A Nikon 50 mm f/1.4AI lens (Nikkor-4759425) was also used with the Photron camera with an f-number of 5.8 set during testing. The camera sensor (CMOS) resolution was 1024 × 464 pixels resulting in an imaged resolution of 84.7 μm/pixel. Laser and

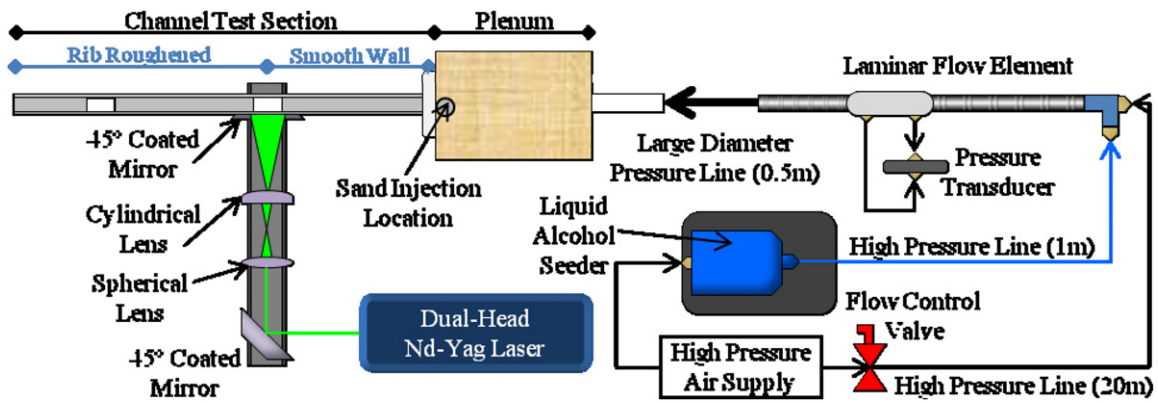


Figure 13. Rib channel facility used to acquire experimental MPF images.

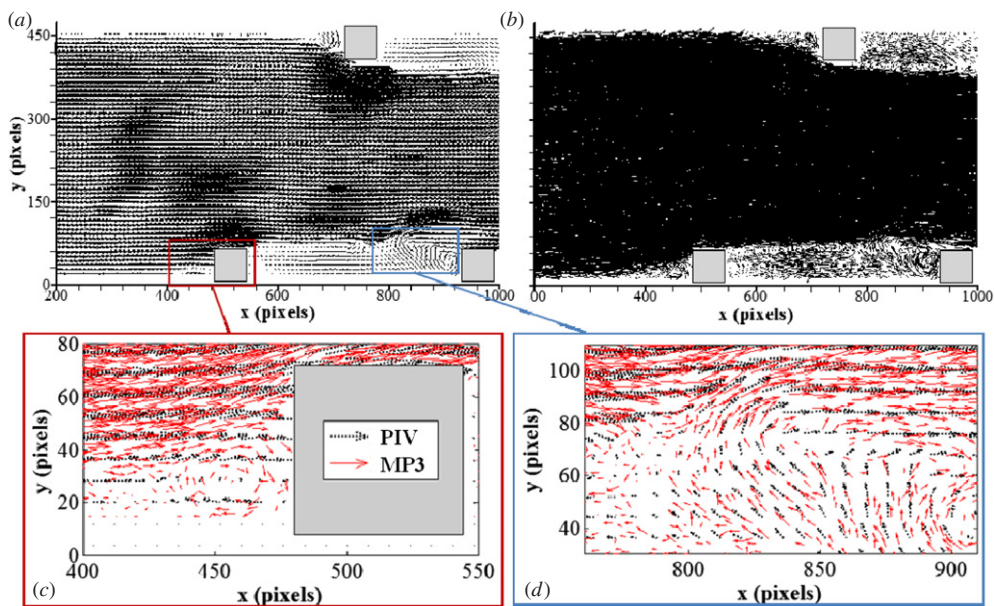


Figure 14. Measured velocity field for the experimental images using (a) PIV and (b) MP3-PTV along with zoomed regions (c) and (d) comparing PIV (black) and MP3-PTV (red) measured trajectories.

camera settings were kept constant for all tests, thus ensuring a consistent image quality for each case. All results presented were averaged over 100 image pairs.

The flowfield was seeded with both tracer and sand particles, resulting in a MPF having a bi-modal distribution of diameters. Tracer seeding was accomplished using an alcohol-based liquid atomizer producing $\sim 1 \mu\text{m}$ diameter droplets which were injected upstream of the LFE, as shown in figure 13, to ensure a homogeneous particles distribution. Arizona Road Dust (AzRD), a commonly used standardized test sand [15], was introduced upstream of the channel inlet from a sealed gravity feed system. The resulting particle size distributions are shown in table 6. Also shown in table 6 are the Stokes numbers of both the tracer and sand particles, based on the rib height and bulk channel velocity. The relative differences in particle size and density allowed for a broad range of particle Stokes numbers.

3.3.2. Performance on single-phase rib-channel flow (tracer particles only). In this section, a comparison of the

Table 6. Particle properties for the MPF experiment.

	Density	Particle diameter (μm)		
	ρ (kg m^{-3})	d_m/St_m	d_{\min}/St_{\min}	d_{\max}/St_{\max}
Alcohol tracers	910	1/0.001		
Sieved AzRD	2650	193/1600	77/256	517/11 540

MP3-PTV to PIV processed results is provided for a rib-channel flow seeded only with tracer particles. The experimental images were processed with the MP3-PTV algorithm using EDT particle identification, CLSG particle sizing and NN- $d-I$ pair-matching methods. PIV processing of the single-phase experimental images was also carried out with the RPC algorithm in a similar manner to the VSJ#301 (see table 3) with three additional post-processing validation passes. A summary of the MP3-PTV processing parameters is given in table 7.

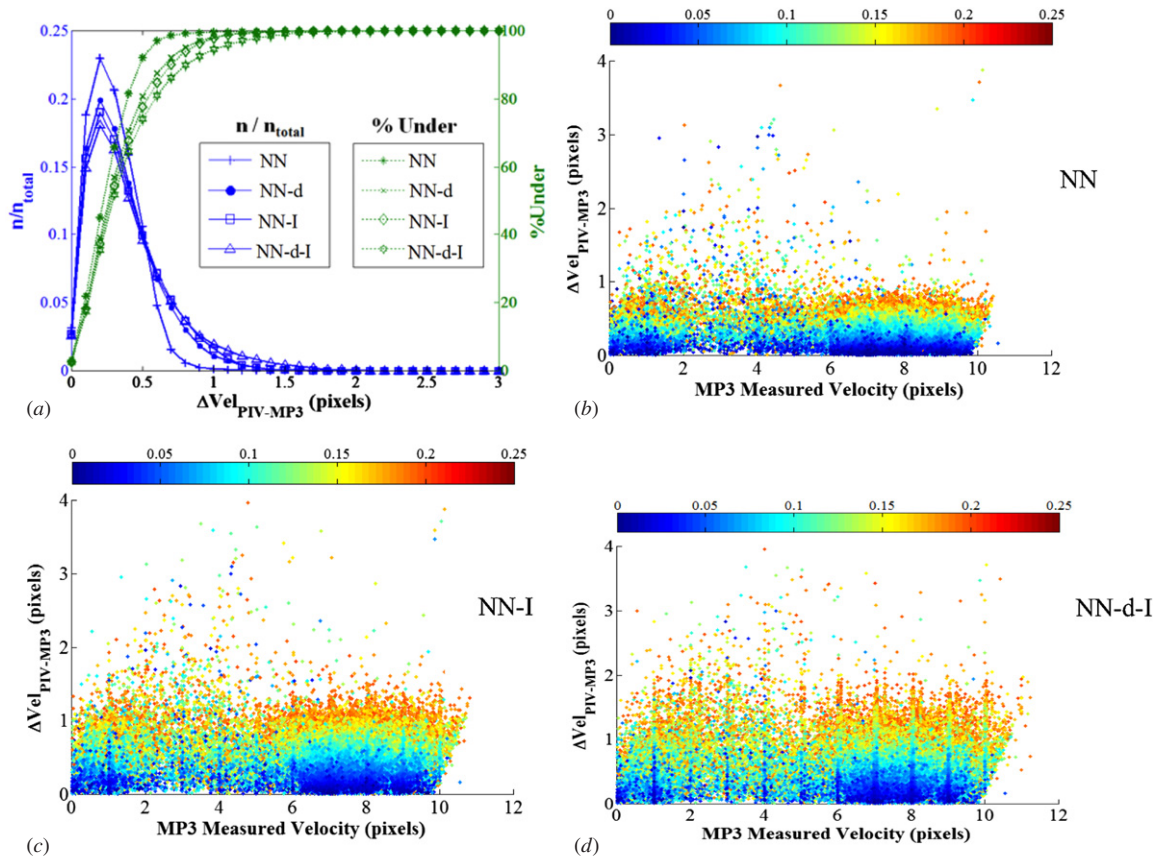


Figure 15. (a) Histogram and cumulative distribution of the difference $\Delta Vel_{PIV-MP3}$ for the different combination of estimation parameters (b) scatter plot of the difference $\Delta Vel_{PIV-MP3}$ colored by the C_{12} as a function of measured displacement for NN only (c) same but for NN-I and (d) same but for NN-d-I.

Table 7. MP3-PTV processing parameters for the experimental set (tracers).

MP3-PTV parameters (tracer only)		Units
ID and sizing method	EDT/CLSG	
I_{th}	20	intensity
σ_S	4	#
W_d, W_i, W_{NN}	1/1/1	#
r_S	3	pixels
PTV validation	3 passes	
Passes 1 and 2 (UOD)	MAD = 2.5	
Pass 3 (C_{12})	$C_{12} < 0.25$	

The MP3-PTV measured particle velocities for a single image pair are shown in figure 14(b), with the flow direction being from left to right and gray regions representing the rib locations. The PIV-derived velocity measurements are also shown in figure 14(a) for the same image pair. The MP3-PTV measurement density was considerably higher than for PIV, with 22 065 and 6853 measurements, respectively. Decreasing the PIV grid spacing to 4×4 pixels produced 27 051 measurements. This increase, however, occurred at a window overlap of $\sim 90\%$, calling into question the independence of each vector. A grid spacing of 8×8 pixels, with a window overlap of 75%, can be acceptable given the high shear regions and turbulent nature of the flowfield although typically even

less overlap is desired, hence PIV would yield an even smaller number of vectors.

Overall the measured velocity fields were comparable, with similar flow structure and velocities exhibited for both the MP3-PTV and PIV. Analysis of the absolute velocity difference between the two methods, $\Delta Vel_{PIV-MP3}$, is shown in figure 15. Comparison of the randomly distributed MP3-PTV measurements and the gridded PIV measurements was accomplished through a bicubic-spline interpolation. The mean difference in the velocity measurements was 0.48 pixels with a standard deviation of 0.41 pixels. From the distribution and cumulative histograms (figure 15(a)) we see that the population of particles with higher deviation from the PIV measurements is increasing with the addition of the second and third estimation parameter. When only NN was used, approximately 95% of the MP3-PTV velocity measurements were within 0.5 pixel of the corresponding PIV measurement, indicating as expected, that the methods were in close agreement. However, once each of, or the combination of, the diameter and intensity are introduced in the estimation, the percentage of measurements within 0.5 pixels drops well under 80%. This increase in deviation illustrates that the multi-parametric approach is able to refine the velocity measurement otherwise dictated solely by NN of the PIV velocity by choosing particles that are a better match. Figures 15(b)–(d) further illustrate this effect but plotting the $\Delta Vel_{PIV-MP3}$ colored by C_{12} . We observe that the use of the

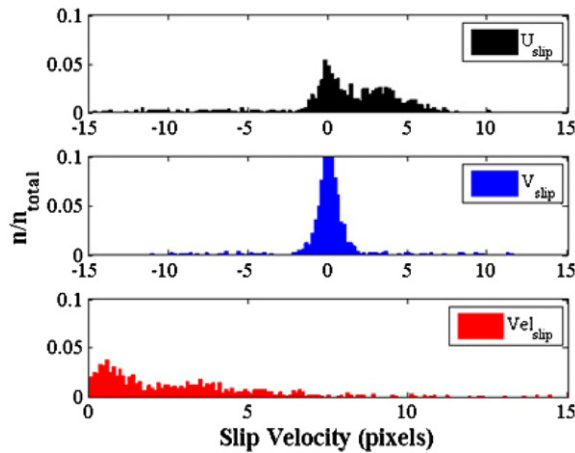


Figure 16. Histogram of particle slip velocities of the sand particles as compared to the simultaneously resolved tracer particle velocities.

Table 8. MP3-PTV processing parameters for the experimental set (sand).

MP3-PTV parameters (sand)		Units
ID and sizing method	EDT/CLSG	
I_{th}	30	intensity
σ_S	4	#
W_d, W_i, W_{NN}	1/1/1	#
r_S	15	pixels
PTV validation	none	

additional matching parameters expands the difference range for measurements with $C_{12} < 0.1$ as intensity (figure 15(c)) and diameter (figure 15(d)) are included. In addition, a small biasing toward integer C_{12} values was observed in figure 15(d). The biasing resulted from the very small imaged tracer particle size, which adversely affected the particle's subpixel diameter estimation. However, this effect does not introduce peak-locking on the PTV velocity estimation.

3.3.3. Performance on multiphase rib-channel flow (tracer and sand particles). In this section, results are provided for a rib-channel flow simultaneously seeded with both tracers and sand particles. All images initially underwent a background subtraction, which was equal to the minimum intensity value registered for each pixel over all images within a single test case. This image pre-processing step assured a uniform background level and also equilibrated any intensity variation between the laser pulses. The experimental images were then processed with the MP3-PTV algorithm using EDT particle identification and CLSG particle sizing (see tables 7 and 8). Given that the motions of both particle populations were simultaneously resolved, the instantaneous slip velocities of the sand particles could be measured directly through a distance-weighted spatial average of the neighboring tracer velocities.

Normalized histograms of the measured slip velocities of the sand particles are shown in figure 16. Given the unsteady and turbulent nature of the rib-channel flow and the high Stokes number of the sand particles, the broad distribution

of slip velocities measured was not unexpected. The average particle slip velocity, however, was still $\sim 50\%$ of the bulk velocity indicating that the sand particle trajectories were not completely ballistic.

4. Conclusions

Systematic testing of the MP3-PTV algorithm on a multitude of data sets illustrated the benefits of combining additional pair-matching parameters, such as diameter and maximum intensity, with traditional PTV. The contribution of each step in the MP3-PTV was also individually evaluated with attention paid to performance and error of the velocity measurements.

Regarding particle identification and segmentation, the presented EDT outperformed the SVT by a factor of 2 or more. For the VSJ#301 image set, processing with the EDT resulted in the highest number of correctly identified and segmented particles compared to all other published results. Of the six sizing methods evaluated, the CLSG resulted in the most robust estimate of particle centroid, diameter and true intensity. Identifying particles with the EDT reduced the error of all sizing methods, especially for the IWC, which was the most computationally efficient method. Providing a displacement estimate for the particles increased vector reliability. For a single population of particles (i.e. single-phase flow), all evaluated estimation methods performed similarly indicating that the accuracy of the preconditioning method was more important than its application. For a multiphase flowfield, the MP3-PTV method out-performed traditional and hybrid PTV, especially when processing unsegregated images.

Application of the MP3-PTV algorithm on real-world experimental images further confirmed the capabilities of the method. The effectiveness of the MP3-PTV was demonstrated on a simultaneously seeded MPF having a dilute solid-gas mixture of sand particles and dry air. Therein lies the main strength of utilizing the MP3-PTV algorithm, which facilitated the time-resolved measurement of slip velocities either with or without segregation and separation of the particle populations.

References

- [1] Adrian R J 2005 Twenty years of particle image velocimetry *Exp. Fluids* **39** 159–69
- [2] Adrian R J and Yao C-S 1985 Pulsed laser technique application to liquid and gaseous flows and the scattering power of seed materials *Appl. Opt.* **24** 44–52
- [3] Bachalo W D 1994 Experimental methods in multiphase flows *Int. J. Multiph. Flow* **20** 261–95
- [4] Bachalo W D and Houser M J 1984 Phase Doppler spray analyzer for simultaneous measurements of drop size and velocity distributions *Opt. Eng.* **23** 583–90
- [5] Baek S J and Lee S J 1996 A new two-frame particle tracking algorithm using match probability *Exp. Fluids* **22** 23–32
- [6] Black D L, McQuay M Q and Bonin M P 1996 Laser-based techniques for particle-size measurement: a review of sizing methods and their industrial applications *Prog. Energy Combust. Sci.* **22** 267–306
- [7] Brady M R, Raben S G and Vlachos P P 2009 Methods for digital particle image sizing (DPIS): comparisons and improvements *Flow Meas. Instrum.* **20** 207–19

- [8] Cardwell N, Vlachos P and Thole K 2010 Developing and fully developed turbulent flow in ribbed channels *Exp. Fluids* **50** 1357–71
- [9] Cheng Y, Pothos S and Diez F 2010 Phase discrimination method for simultaneous two-phase separation in time-resolved stereo PIV measurements *Exp. Fluids* **49** 1375–91
- [10] Cowen E A and Monismith S G 1997 A hybrid digital particle tracking velocimetry technique *Exp. Fluids* **22** 199–211
- [11] Eckstein A and Vlachos P P 2009 Assessment of advanced windowing techniques for digital particle image velocimetry (DPIV) *Meas. Sci. Technol.* **20** 075402
- [12] Eckstein A and Vlachos P P 2009 Digital particle image velocimetry (DPIV) robust phase correlation *Meas. Sci. Technol.* **20** 055401
- [13] Hassan Y A, Blanchat T K and Seeley C H 1992 PIV flow visualization using particle tracking techniques *Meas. Sci. Technol.* **3** 633–42
- [14] Hassan Y A and Canaan R E 1991 Full-field bubbly flow velocity measurements using a multiframe particle tracking technique *Exp. Fluids* **12** 49–60
- [15] ISO 1997 Road vehicles—test dust for filter evaluation—part 1. Arizona test dust ISO 12103-1 (Geneva, Switzerland)
- [16] Jones A R 1999 Light scattering for particle characterization *Prog. Energy Combust. Sci.* **25** 1–53
- [17] Keane R D, Adrian R J and Zhang Y 1995 Super-resolution particle imaging velocimetry *Meas. Sci. Technol.* **6** 754–68
- [18] Khalitov D A and Longmire E K 2002 Simultaneous two-phase PIV by two-parameter phase discrimination *Exp. Fluids* **32** 252–68
- [19] Kiger K T and Pan C 2000 PIV technique for the simultaneous measurement of dilute two-phase flows *J. Fluids Eng.* **122** 811–8
- [20] Kim H B and Lee S J 2002 Performance improvements of two-frame particle tracking velocimetry using a hybrid adaptive scheme *Meas. Sci. Technol.* **13** 573–82
- [21] Kobayashi T, Saga T, Segawa S and Knada H 1989 Development of a real-time velocity measurement system for two-dimensional flow fields using a digital image processing technique *Trans. JSME B* **55** 107
- [22] Marxen M, Sullivan P E, Loewen M R and Jahne B 2000 Comparison of Gaussian particle center estimators and the achievable measurement density for particle tracking velocimetry *Exp. Fluids* **29** 145–53
- [23] Mikheev A V and Zubtsov V M 2008 Enhanced particle-tracking velocimetry (EPTV) with a combined two-component pair-matching algorithm *Meas. Sci. Technol.* **19** 085401
- [24] Nishino K, Kato H and Torii K 2000 Stereo imaging for simultaneous measurement of size and velocity of particles in dispersed two-phase flow *Meas. Sci. Technol.* **11** 633–45
- [25] Nogueira J, Lecuona A and Rodriguez P A 1997 Data validation, false vectors correction and derived magnitudes calculation on PIV data *Meas. Sci. Technol.* **8** 1493–501
- [26] Ohmi K and Lam D H 1998 New particle tracking PIV using an improved relaxation method *Proc. 8th Int. Symp. on Flow Visualization*
- [27] Ohmi K and Li H 2000 Particle-tracking velocimetry with new algorithms *Meas. Sci. Technol.* **11** 603–16
- [28] Okamoto K, Nishio S, Kobayashi T, Saga T and Takehara K 2000 Evaluation of the 3D-PIV standard images (PIV-STD Project) *J. Vis.* **3** 115–23
- [29] Okamoto K, Nishio S, Saga T and Kobayashi T 2000 Standard images for particle-image velocimetry *Meas. Sci. Technol.* **11** 685–91
- [30] Pun C S, Susanto A and Dabiri D 2007 Mode-ratio bootstrapping method for PIV outlier correction *Meas. Sci. Technol.* **18** 3511–22
- [31] Ruhnau P, Guetter C, Putze T and Schnorr C 2005 A variational approach for particle tracking velocimetry *Meas. Sci. Technol.* **16** 1449–58
- [32] Takehara K, Adrian R J, Etoh G T and Christensen K T 2000 A Kalman tracker for super-resolution PIV *Exp. Fluids (Suppl.)* **29** S034–41
- [33] Takehara K and Etoh T 1998 A study on particle identification in PTV particle mask correlation method *J. Vis.* **1** 313–23
- [34] Uemura T, Yamamoto F and Ohmi K 1989 A high speed algorithm of image analysis for real time measurement of two-dimensional velocity distribution *ASME FED-85* pp 129–34
- [35] Wernet M P 1993 Fuzzy logic particle-tracking velocimetry *Proc. SPIE* **2005** 701–8
- [36] Westerweel J 1994 Efficient detection of spurious vectors in particle image velocimetry *Exp. Fluids* **16** 236–47
- [37] Westerweel J 1997 Fundamentals of digital particle image velocimetry *Meas. Sci. Technol.* **8** 1379–92
- [38] Westerweel J and Scarano F 2005 Universal outlier detection for PIV data *Exp. Fluids* **39** 1096–100
- [39] Willert C E and Gharib M 1991 Digital particle image velocimetry *Exp. Fluids* **10** 181–93
- [40] Yamamoto F, Uemura T, Tian H and Ohmi K 1993 Three-dimensional PTV based on binary cross-correlation method *JSME Int. J.* **36** 279–84